Journal of Materials Chemistry C

ROYAL SOCIETY OF CHEMISTRY

PAPER

View Article Online
View Journal | View Issue

Cite this: J. Mater. Chem. C, 2023, 11, 10221

Multifunctional optical sensing platform of temperature, pressure (vacuum) and laser power density: $NaYF_4$: Gd^{3+}, Yb^{3+}, Er^{3+} nanomaterial as luminescent thermometer, manometer and power meter†

Christian Hernández-Álvarez, *[a] Gabriela Brito-Santos, [b] Inocencio R. Martín, [a] Joaquín Sanchiz, [b] Kamel Saidi, [c] Kevin Soler-Carracedo, [a] Łukasz Marciniak [d] and Marcin Runowski *[ae]

Temperature and pressure are crucial physical parameters in materials science, hence their monitoring is especially important for scientists and engineers. Moreover, the on-target power density parameter is often underestimated, and in various real applications it is difficult to determine it correctly using conventional contact power meters. We developed for the first time, a multi-functional sensing platform allowing ratiometric optical detection of pressure (vacuum), temperature and excitation power density, using a sensor based on the upconverting inorganic nanomaterial ($NaYF_4$: Gd^{3+}, Yb^{3+}, Er^{3+}) emitting in the visible range upon NIR laser excitation. The monotonic dependency between the temperature and the luminescence intensity ratio of the Er^{3+} thermally-coupled levels (TCLs), *i.e.* the intensity ratio of the band (525/550 nm), allows to monitor the temperature and laser-induced heating observed under vacuum conditions in the sample, so it is possible to use as a remote vacuum sensor. Moreover, the temperature elevation induced by increasing of the laser power also allows to use it as an optical power density meter. We believe that this work can inspire new research directions that will enable the development of the multi-functional sensor materials.

Received 17th May 2023,
Accepted 22nd June 2023

DOI: 10.1039/d3tc01712e

rsc.li/materials-c

Introduction

There are many crucial physical parameters in materials science, among them, temperature and pressure are of great importance in a wide range of scientific research and industrial operations.[1–9] For this reason, fast, accurate and remote measurements have increasingly attracted the attention of researchers.[3–7,10,11] For measurements of these two parameters remotely, is usually used the optical techniques based on organic complexes, d-block metal ions and on the luminescence of lanthanides are usually used.[3–7,10–14] In addition, working with variable laser power involves an additional difficulty in various non-linear optical measurements, trying to get the exact spot size and determine the on-target power density.[15]

The great interest in lanthanide (Ln) ions for optical methods is due to their wide variety of useful spectroscopic properties, among them wide-range multicolor emission, long short Stokes shift, luminescence lifetimes, narrow emission lines, *etc.*, all this properties are related with the 4f–4f electronic transitions.[3–7,16–20] Other advantage that have the inorganic materials doped with lanthanide ions is the good responses to pressure and temperature, so they can function as luminescent manometers and thermometers.[3–7,10–13] Although, there are currently not many pumping power sensors, so their use as power meters is limited, for the moment.[20,21] Materials containing Nd^{3+}, Er^{3+} and Tm^{3+} are commonly used as luminescent thermometers for temperature sensing. This is due to the presence of thermally coupled levels (TCL) that are separated by a small energy difference

[a] Universidad de La Laguna, Departamento de Física, MALTA-Consolider Team, IMN and IUdEA Apdo. Correos 456, E-38206, San Cristóbal de La Laguna, Santa Cruz de Tenerife, Spain. E-mail: mrunowsk@ull.edu.es, chernaal@ull.edu.es; Tel: +34 922316502 (6061), +34 922316502 (6918)
[b] Departamento de Química, Facultad de Ciencias, Apdo. Correos 456, E-38200, San Cristóbal de La Laguna, Santa Cruz de Tenerife, Spain
[c] Laboratoire de Physique Appliquée, Groupe des Matériaux Luminescents, Faculté des Sciences de Sfax, Département de Physique, Université de Sfax, BP 1171 Sfax, Tunisia
[d] Institute of Low Temperature and Structure Research, Polish Academy of Sciences, Okólna 2, 50-422 Wrocław, Poland
[e] Adam Mickiewicz University, Faculty of Chemistry, Uniwersytetu Poznańskiego 8, 61-614 Poznań, Poland. E-mail: runowski@amu.edu.pl

† Electronic supplementary information (ESI) available. See DOI: https://doi.org/10.1039/d3tc01712e

(approximately 50–2000 cm^{-1}). As a result, the emission from these materials follows a Boltzmann-type behavior.[3,4,6,7,10–13,22–25] On the other hand, to measure the laser (pump) power density, one already reported approach is to use materials containing Cr^{3+} ions, which exhibit well-defined laser-induced self-heating behaviour, directly affecting the luminescence intensity ratio (local variation of temperature) that occurs between the $^4T_{2(g)}$ level and the $^2E_{(g)}$ level.[21] For pressure sensing, inorganic materials are typically used, mainly thanks to their high structural stability and resistance to compression–decompression cycles. For the optical monitoring of high pressure systems, the characteristic emissions of the Eu^{2+} and Sm^{2+} ions embedded in different inorganic matrices are very sensitive to pressure changes.[26–29] These materials are good alternative to the fluorescent ruby sensor (Al_2O_3:Cr^{3+}), whose emission is highly temperature dependent.[30–32] On the other hand, for low pressure (vacuum), it is possible to employ inorganic materials that exhibit a light-to-heat conversion by pressure-modulated or organic complexes (dyes) that demonstrate oxygen-dependent quenching of emission, in which luminescence thermometry controls heating–cooling processes.[10,11,33,34] However, oxygen-sensitive organic dyes have a limited range of pressure where they detect, typically from ≈0.05 to 2 bar,[34] so the latter ones seem to be a better alternative for vacuum sensing in a broader range (≈10^{-5}–1 bar).

In luminescence thermometry, there are several approaches which allow the development of optical thermometers of micrometric or nanometric size, working in a wide temperature range.[6,12,13,22–25,35–37] They typically exploit changes in luminescence lifetimes or band intensity ratio of two excited levels to determine temperature.[6,12,13,20,23,35–41] In addition, optical pressure sensors have the ability to operate over a wide range from vacuum to high pressure.[3–5,7,10,11,41] Because their operating mechanisms are different, *i.e.* high-pressure sensors are based on material compression, which directly affects the spectroscopic properties of optically active ions, such as changes in lifetimes, emission line width, luminescence band intensity ratios or line shift.[2–5,7,41] On the other hand, low-pressure luminescent sensors (operating below 1 bar) utilize the loss of concentration of gas molecules, which directly affects the local temperature rise or the quenching of luminescence (emission intensity variations), this discovery enables the design of vacuum sensors using the luminescent thermometers/heaters, this view is based on the effect of laser heating of materials, which is enhanced in vacuum conditions.[10,11,33,34]

In this work, we show that $NaYF_4$: Gd^{3+}, Yb^{3+}, Er^{3+}, nanomaterial can be used as a multifunctional detector for temperature and pressure using the vacuum-enhanced light-to-heat conversion (see Fig. 1(a)).[42] The developed sensor can operate in a temperature range from 300 to 600 K and in a pressure

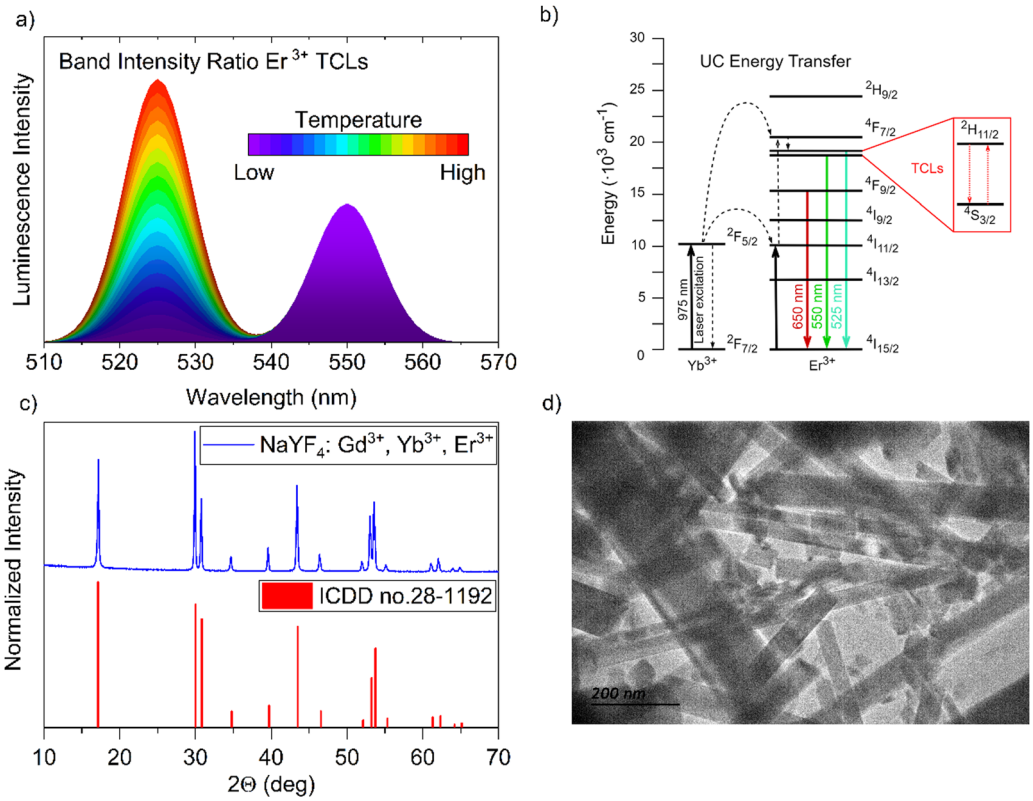

Fig. 1 (a) Concept of temperature-dependent emission bands in Er^{3+}-doped luminescent materials. (b) Er^{3+} and Yb^{3+} ion energy level diagram illustrating the principal processes occurring in the system, focusing on Er^{3+} TCLs $^2H_{11/2}$ and $^4S_{3/2}$. (c) comparison of the XRD pattern of the synthesized $NaYF_4$:Gd^{3+}, Yb^{3+}, Er^{3+} nanomaterial with the reference data. (d) representative TEM image of the obtained $NaYF_4$:Gd^{3+}, Yb^{3+}, Er^{3+} nanoparticles crystallizing in a hexagonal structure.

range from $\approx 10^{-4}$ to 1 bar. In addition, this material can be used as a power density detector using two different approaches, *i.e.* the change in the band intensity ratio of Er^{3+} TCLs is due to the local temperature change induced with laser heating, as well as by utilizing the well-defined and non-linear variation of upconversion (UC) emissions, which depends on the laser power density used. Please note, that the first strategy is valid in the high-power range ($\approx$5–850 W cm^{-2}) and the second method can be used operating in a low-power density regime ($\approx$0.2–200 W cm^{-2}).

Results and discussion

Characteristics of the sensor material

The luminescent sensor material based on the nano-sized $NaYF_4$ particles, co-doped with 78% of Y^{3+} and doped with a 10% of Yb^{3+}, 10% of Gd^{3+} and 2% of Er^{3+} ions, was obtained through the modified hydrothermal synthesis method described by Zhang *et al.*[43] The investigated fluoride nanomaterial is optically active and exhibits non-linear response to the excitation light, *i.e.* the anti-Stokes emission of Er^{3+}, that is commonly observed in material with Yb^{3+}–Er^{3+} ions, can generate UC luminescence when the sample is excitated by laser irradiation ($\approx$975 nm). In such systems, the Yb^{3+} ("light-harvesting ions") absorbs the radiation of the incident laser and transfer it to the neighboring Er^{3+} ions (emitters), causing an UC energy transfer process (energy level diagram in Fig. 1(b)).[4,10,38] The use of Gd^{3+} ions allows lowering the reaction temperature during the synthesis process, ensuring the formation of the desired crystal structure.[44]

The synthesized nanomaterial crystallizes in a hexagonal crystal system, $P\bar{6}$ space group, and its XRD pattern agrees well with the reference data from the ICDD database (International Centre for Diffraction Data), of hexagonal β-$NaYF_4$ (card no. 28-1192)[45] as can be seen in Fig. 1(c). The low phonon energy of its crystal lattice, *i.e.* $\approx$370 cm^{-1},[46,47] reduces the probability of nonradiative excited states depopulation, facilitating the generation of efficient UC luminescence.[48] Fig. 1(d) shows the transmission electron microscopy (TEM) image of the obtained nanocrystals, revealing their elongated, rod-like shape, with an average width of $\approx$50–100 nm and maximum length reaching up to $\approx$1 μm. These results also agree with the data from the scanning electron microscopy (SEM) shown in the ESI† in Fig. S1. The performed elemental analysis reveals that the atomic concentration of lanthanides in the nanocrystals is consistent with that introduced during the synthesis process in the hydrothermal reactor, as indicated in Table S1 in the ESI† data. It is worth noting, that the material studied is stable under high-temperature condition, up to at least $\approx$700 K, preserving its hexagonal structure.[49]

Temperature sensing

The monotonic thermal change of the band intensity ratio is the results of the thermal coupling between the $^2H_{11/2}$ and $^4S_{3/2}$ states, with $\Delta E \approx 866 \pm 5$ cm^{-1} (value determined from the spectra, using the centroids of the 525 and 550 nm emissions).[6] For the calibration of the UC response from the $NaYF_4$:Gd^{3+}, Yb^{3+}, Er^{3+} sample, its UC emission spectra were measured using a continuous wave 975 nm NIR laser in a range of temperature ($\approx$300–600 K), with power density of $\approx$0.1 W cm^{-2}. Results from

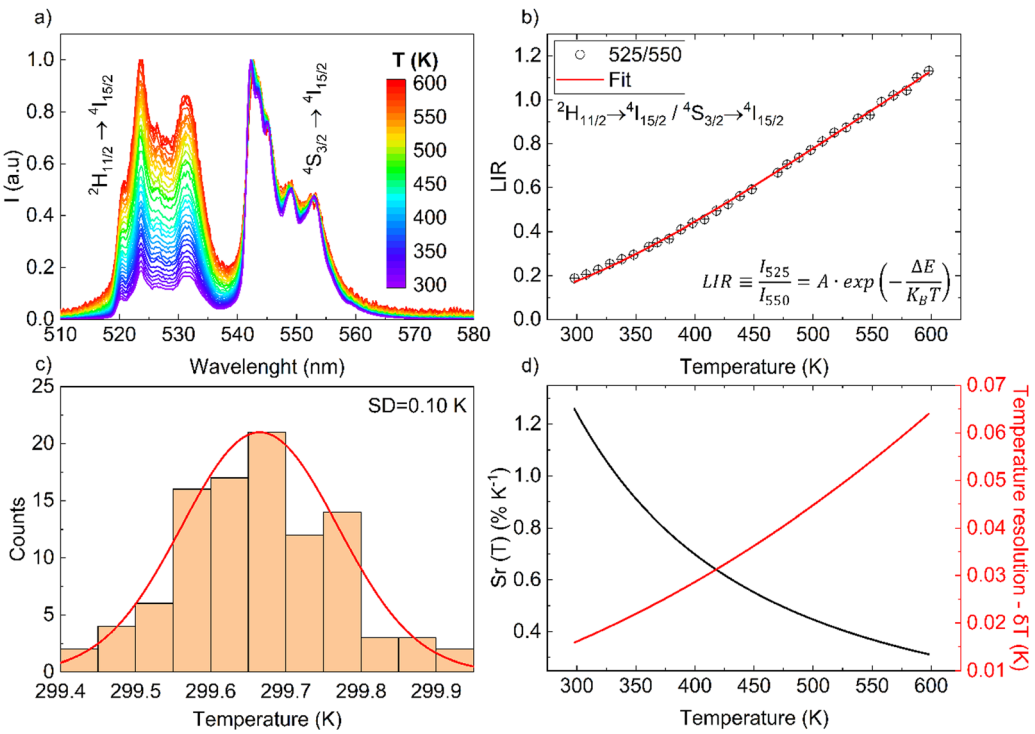

Fig. 2 (a) Normalized UC emission spectra as a function of temperature, measured at λ_{ex} = 975 nm and 0.1 W cm^{-2}. (b) Determined band intensity ratios as a function of temperature. (c) Temperature distribution. (d) Relative sensitivity and Resolution as a function of temperature.

Fig. 2(a) clearly confirms the temperature dependence relationship of the Er^{3+} thermalized bands and their radiative transitions $^2H_{11/2} \rightarrow {}^4I_{15/2}$ ($\approx$525 nm) and $^4S_{3/2} \rightarrow {}^4I_{15/2}$ ($\approx$550 nm), according to the diagram shown in Fig. 1(b). From the recorded spectra, by integrating the area under the bands of interest, the band intensity ratio of 525/550 nm was determined. This band intensity ratio values are plotted in Fig. 2(b) as a function of temperature, and follow Boltzmann-type behavior using the following function:

$$\mathrm{LIR} \equiv \frac{I_{525}}{I_{550}} = A\mathrm{e}^{-\frac{\Delta E}{k_B T}} \quad (1)$$

where LIR is the luminescence (band) intensity ratio (525/550 nm); ΔE is the energy difference between the analyzed excited states; k_B is the Boltzmann constant; T is the absolute temperature; and A is a constant which depends on the states degeneracies, branching ratio of the transitions in relation to the ground state, spontaneous emission rates and energy of the transitions.[6] The performed fitting resulted in $\Delta E \approx 776 \pm 6$ cm^{-1} (most plausibly due to band overlapping this experimental value is lower than that obtained theoretically.), $A \approx 7.28$ and $R^2 \approx 0.99$. To ensure good sensitivity and high accuracy of the optical temperature determination, the remote ratiometric method commonly used in luminescence thermometry was used. In order to compare the performance of different sensors (independently of the measuring setup and thermometric parameter used), it is useful to calculate its relative sensitivity (S_r) given by the formula:

$$S_r(T) = 100\% \times \frac{1}{\mathrm{LIR}} \frac{\mathrm{dLIR}}{\mathrm{d}T} \quad (2)$$

The sensor sensitivity developed depends on the temperature range of interest, *i.e.* $S_r(T)$ parameter varies significantly, and at room temperature it reaches $\approx$1.26% K^{-1} (see Fig. 2(d)), which is high compared to other Er^{3+}-based sensors. The performance comparison of the luminescent thermometer is given in Table 1.

Fig. 2(c) shows a histogram obtained based on the 100 spectra recorded under the same conditions (room temperature), from which a standard deviation of about 0.10 K can be obtained. This value can be used as an estimation of the experimental temperature error which has this temperature sensing method. In addition, a theoretical estimation of the temperature resolution δT can be also calculated using equation:

$$\delta T = \frac{1}{S_r} \frac{\delta \mathrm{LIR}}{\mathrm{LIR}} \quad (3)$$

where δLIR is the uncertainty of determination of the band intensity ratio 525/550 nm and is estimated from the LIR error in the 100 measurements.[6] It can be seen that the theoretical error at room temperature is $\approx$0.01 K, which is smaller than the experimental value of $\approx$0.10 K (more reliable). As expected,

Table 1 Comparison of performance of different luminescent thermometers (Er^{3+}-based), power density meters and optical vacuum sensors

Thermometers

Host	Emitting ion	Relative sensitivity $S_r(T)$ [% K^{-1}]	Transitions	λ [nm]	Ref.
$NaYF_4$	Er^{3+}	1.26	$^2H_{11/2} \rightarrow {}^4I_{15/2}/{}^4S_{3/2} \rightarrow {}^4I_{15/2}$	525/550	This work
β-$NaYF_4$/SiO_2 core/shell nanorods	Er^{3+}	1.31	$^2H_{11/2} \rightarrow {}^4I_{15/2}/{}^4S_{3/2} \rightarrow {}^4I_{15/2}$	525/550	54
YF_3-modified cellulose fibers	Er^{3+}	1.2	$^2H_{11/2} \rightarrow {}^4I_{15/2}/{}^4S_{3/2} \rightarrow {}^4I_{15/2}$	525/550	55
$BaTiO_3$	Er^{3+}	1.21	$^2H_{11/2} \rightarrow {}^4I_{15/2}/{}^4S_{3/2} \rightarrow {}^4I_{15/2}$	525/550	56
Y_2SiO_5	Er^{3+}	0.7	$^2H_{11/2} \rightarrow {}^4I_{15/2}/{}^4S_{3/2} \rightarrow {}^4I_{15/2}$	525/550	57
Gd_2O_3–AuNP	Er^{3+}	0.72	$^2H_{11/2} \rightarrow {}^4I_{15/2}/{}^4S_{3/2} \rightarrow {}^4I_{15/2}$	525/550	58
La_2CaZnO_5	Er^{3+}	0.71	$^2H_{11/2} \rightarrow {}^4I_{15/2}/{}^4S_{3/2} \rightarrow {}^4I_{15/2}$	525/550	59
$Y_2Mo_3O_{12}$	Er^{3+}	0.79	$^2H_{11/2} \rightarrow {}^4I_{15/2}/{}^4S_{3/2} \rightarrow {}^4I_{15/2}$	525/550	60
YVO_4	Er^{3+}	0.8	$^2H_{11/2} \rightarrow {}^4I_{15/2}/{}^4S_{3/2} \rightarrow {}^4I_{15/2}$	525/550	10

Power density meters

Host	Emitting ion	Relative sensitivity $S_r(I)$ [% W^{-1} cm^2]	Transitions	λ (nm)	Ref.
$NaYF_4$	Er^{3+}	0.46	$^2H_{11/2} \rightarrow {}^4I_{15/2}/{}^4S_{3/2} \rightarrow {}^4I_{15/2}$	525/550	This work
		835	$^2H_{11/2} \rightarrow {}^4I_{15/2}$	525	
$GdAl_3(BO_3)_4$	Cr^{3+}	0.07	$^2E \rightarrow {}^4A_2/{}^4T_2 \rightarrow {}^4A_2$	750/690	21

Optical vacuum sensors

Host	Emitting ion	Relative sensitivity $S_r(T)$ [% mbar^{-1}]	Transitions	λ (nm)	Ref.
$NaYF_4$	Er^{3+}	20 (at 1 mbar) 1.1 (at 10 mbar)	$^2H_{11/2} \rightarrow {}^4I_{15/2}/{}^4S_{3/2} \rightarrow {}^4I_{15/2}$	525/550	This work
YPO_4	Er^{3+}	10 (at 1 mbar) 1 (at 10 mbar)	$^2H_{11/2} \rightarrow {}^4I_{15/2}/{}^4S_{3/2} \rightarrow {}^4I_{15/2}$	525/550	42
YVO_4	Er^{3+}	40 (at 1 mbar) 1 (at 10 mbar)	$^2H_{11/2} \rightarrow {}^4I_{15/2}/{}^4S_{3/2} \rightarrow {}^4I_{15/2}$	525/550	10
$YAlO_3$ (microsphere)	Nd^{3+}	<0.1 (at 1 mbar)	$^4F_{3/2} \rightarrow {}^4I_{9/2}$	914	11
PtTFPL	Organic complex	$\approx$0.1	Triplet $\rightarrow$ singlet	740	53
PtTFPL	Organic complex	$\approx$0.1	Triplet $\rightarrow$ singlet	650	61

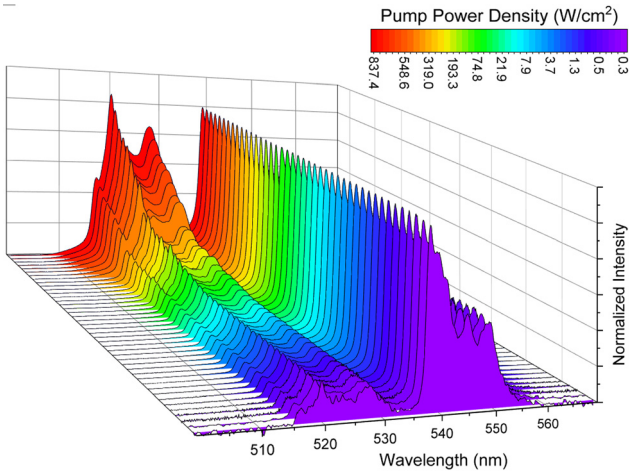

Fig. 3 Normalized UC emission spectra as a function of of pump power density of the $NaYF_4$:Gd^{3+}, Yb^{3+}, Er^{3+} material, measured at λ_{ex} = 975 nm.

according to Fig. 2(d), when the temperature increases, the error and therefore the uncertainty of temperature determination grows, which can be explained in terms of the reduction of the signal-to-noise ratio and S_r values with temperature.

Optical power density meter

Next, the UC emission spectra were measured as a function of laser power density (0.27–930 W cm^{-2}) at ambient conditions (Fig. 3). As can be seen, the LIR parameter starts to significantly increase at pump power values above ≈10 W cm^{-2} (Fig. 4(a)). The increase in laser power density directly influences local temperature of the sample (see Fig. S2, ESI†), as it can be seen by correlating the LIR values determined from the temperature measurements (Fig. 2(b)) with the LIR values obtained from the measurements performed as a function of laser power (Fig. 4(a)). The monotonic change of LIR in the ≈5–850 W cm^{-2} optical power density range reveals wide operating range of the power meter based on $NaYF_4$:Gd^{3+}, Yb^{3+}, Er^{3+}. In a similar way to the previous study, the main parameters that characterize the sensor performance are the relative sensitivity and the

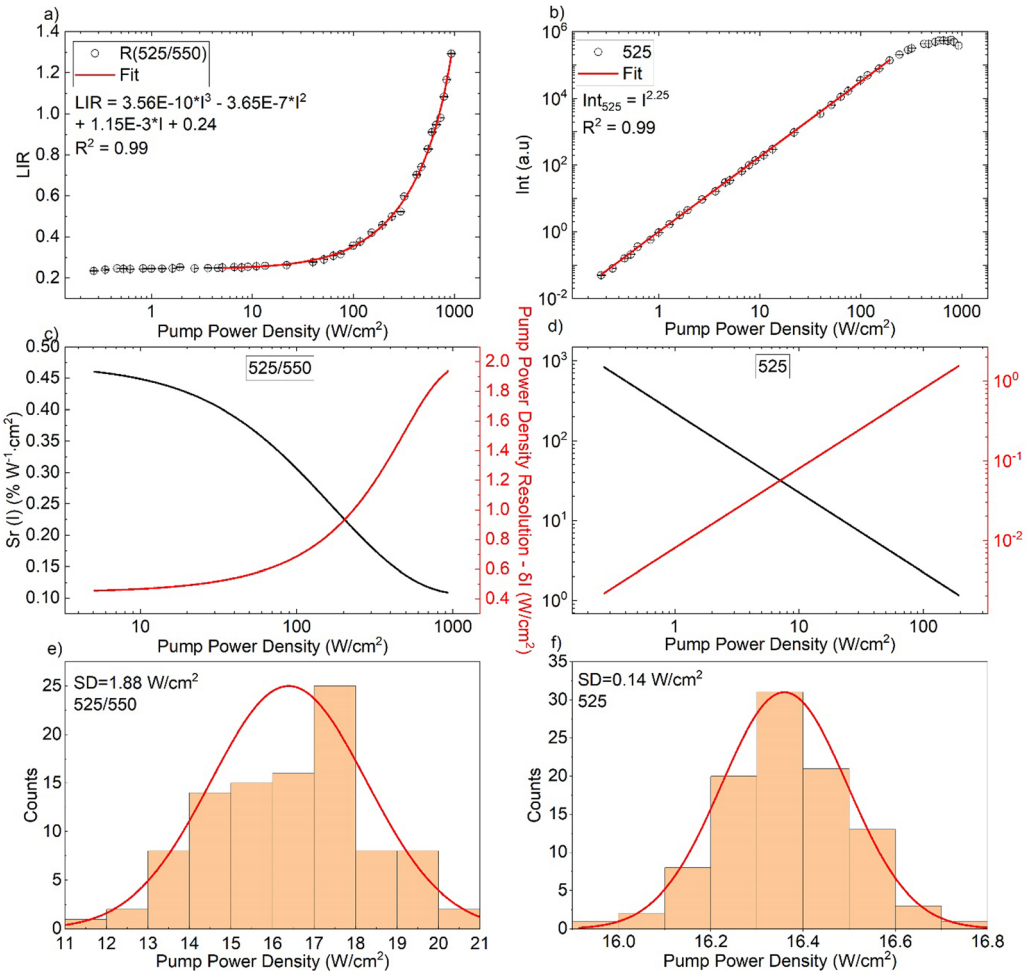

Fig. 4 (a) Determined band intensity ratios of 525/550 nm as a function of pump power density (I). (b) Intensity of the 525 nm as a function of pump power density. (c), (d) The corresponding sensitivity and resolution density. (e), (f) Histograms showing the determined pump power density distributions (experimental resolutions) for the LIR- (e) and intensity-based sensing modes (f).

sensing resolution for pump power density, which can be calculated as:

$$S_r(I) = 100\% \times \frac{1}{\mathrm{LIR}} \frac{\mathrm{dLIR}}{\mathrm{d}I} \quad (4)$$

and

$$\delta(I) = \frac{1}{S_r(I)} \frac{\delta\mathrm{LIR}}{\mathrm{LIR}} \quad (5)$$

With respect to the $S_r(I)$, the available literature data related to power meter is very restricted. (see Table 1). Depending on the excitation power density range of interest, using the 525/550 nm band ratio the $S_r(I)$ varies between $\approx$0.46 and 0.1% W^{-1} cm^2 (see Fig. 4(c)), which is higher than for the first optical power density meter reported by Marciniak *et al.*[21] Moreover, in order to broaden the operating range and improve the relative sensitivity of the sensor at low power densities, we have proposed another sensing method. Namely, the non-linear variation of the 525 nm band intensity with the laser power has been analyzed and plotted in Fig. 4(b). The corresponding $S_r(I)$ and $\delta(I)$ parameters for this approach can be obtained as follows:

$$S_r(I) = 100\% \times \frac{1}{\mathrm{Int}_{525}} \frac{\mathrm{dInt}_{525}}{\mathrm{d}I} \quad (6)$$

and

$$\delta(I) = \frac{1}{S_r(I)} \frac{\delta\mathrm{Int}_{525}}{\mathrm{Int}_{525}} \quad (7)$$

where Int_{525} is the intensity and $\delta\mathrm{Int}_{525}$ is the uncertainty of determination of the 525 nm band intensity. The calculated intensity values of the 525 nm band *vs.* the pump power density (plotted in log–log representations if Fig. 4(b)) show a clear and linear behaviour, starting from $\approx$0.27 W cm^{-2} and ending around 200 W cm^{-2}, which is also the operating range for this sensing mode. The further change of this tendency (plateau observed around 500 W cm^{-2}) is most plausibly due to the saturation effect, which is typically observed for UC luminescence, as well as due to the increasing laser-induced heating of the sample in the high power regime.[50–52] A very high relative sensitivity of the intensity-based parameter obtained in the low power range, *e.g.* $S_r(I) \approx$ 835% W^{-1} cm^2 at 0.27 W cm^{-2} (see Fig. 4(d)), compensates the lack of sensitivity of the LIR-based sensing method in this range. It should be kept in mind, that any deviations in the laser power, as well as scattering and reabsorption effects of the incident photons (in the sample is immersed in any non-transparent medium) can affect the intensity of the emission band, affecting the optical readouts of the power density. It can be seen from the histograms (Fig. 4(e) and (f)) that for a selected power density of $\approx$16 W cm^{-2} the experimental error for the LIR-based sensing method. For the intensity-based one, are $\approx$1.88 and 0.14 W cm^{-2}, respectively. Similarly, like in the case of temperature sensing, the experimentally determined uncertainties for the power density readouts (sensing resolution) are larger than the theoretically estimated values.

Low pressure (vacuum) sensing

For the pressure, a set of UC spectra has been measured using a fixed laser ($\approx$20 W cm^{-2}) and at different vacuum levels (see Fig. 5(a)). The TCLs of Er^{3+} associated with the ratio of band intensities (525/550 nm) clearly increase with changes in the vacuum level of the system (1000–0.07 mbar), as can be seen in Fig. 5(a) and (b), confirming the postulated enhancement of light-heat conversion under vacuum conditions (see Fig. S3, ESI†). While at ambient pressure, the abundant concentration of air molecules (cooling gas) transfers the generated heat to the surroundings, under vacuum conditions the amount of air molecules is limited significantly, for this reason the sample heats up because the heat dissipation (convection) is less efficient.[42]

The determined LIR values are plotted in Fig. 5(b) in logarithmic representation, and correlated with the vacuum level of the system, from 0.33 to 1000 mbar (R^2 = 0.99), using a logistic fit. The relative sensitivity and pressure resolution were estimated based on the following equations:

$$S_r(P) = 100\% \times \frac{1}{\mathrm{LIR}} \frac{\mathrm{dLIR}}{\mathrm{d}P} \quad (8)$$

and

$$\delta P = \frac{1}{S_r} \frac{\delta\mathrm{LIR}}{\mathrm{LIR}} \quad (9)$$

The Fig. 5(d) presents the calculated relative pressure sensitivity $S_r(P)$ and the resolution of pressure sensing δP. For the pressure reduction, the value of $S_r(P)$ increase, begins at atmospheric pressure with 3 $\times$ $10^{-4\%}$ $mbar^{-1}$ and up to $\approx$40% $mbar^{-1}$ (at around 0.3 mbar).

Finally, with the available literature data in Table 1, we have compared the performance of the developed luminescent sensor, but the data of vacuum sensors are very limited for those working at low pressure, *i.e.* around 0.1 mbar. The sensitivity of the sensor depend of the pressure range of interest, *i.e.* around 1 mbar, if we compare the $S_r(P)$ values, from the different sensors, our sensor have $\approx$20% $mbar^{-1}$, this is lower compared to the YVO_4,[10] but higher compared to the YPO4 sensor,[42] $YAlO_3$ perovskite-based sensor (microsphere),[11] or organic sensors.[53] However, at a pressure of around 10 mbar, the developed sensor has $S_r(P) \approx$ 1.1% $mbar^{-1}$, approximately the same as for the vanadate (perovskite sensor does no operate in this range) and the phosphate sensor. Nonetheless, the proposed sensor can be used with acceptable resolution in the range of 0.33–100 mbar, as shown in Fig. 5(d).

Conclusion

In this work, we have demonstrated for the first time the use of lanthanide-doped UC nanomaterial ($NaYF_4$:Gd^{3+}, Yb^{3+}, Er^{3+}) as a multifunctional optical sensor of temperature, laser power density and pressure (vacuum), operating in the visible range upon NIR excitation at 975 nm. The detection of these three parameters (T, I, P) is based on heating the UC material and using the Er^{3+} band intensity ratio (525/550 nm) as a sensing parameter. The applied detection methods provide good sensitivity of optical monitoring of temperature ($\approx$300–600 K), laser

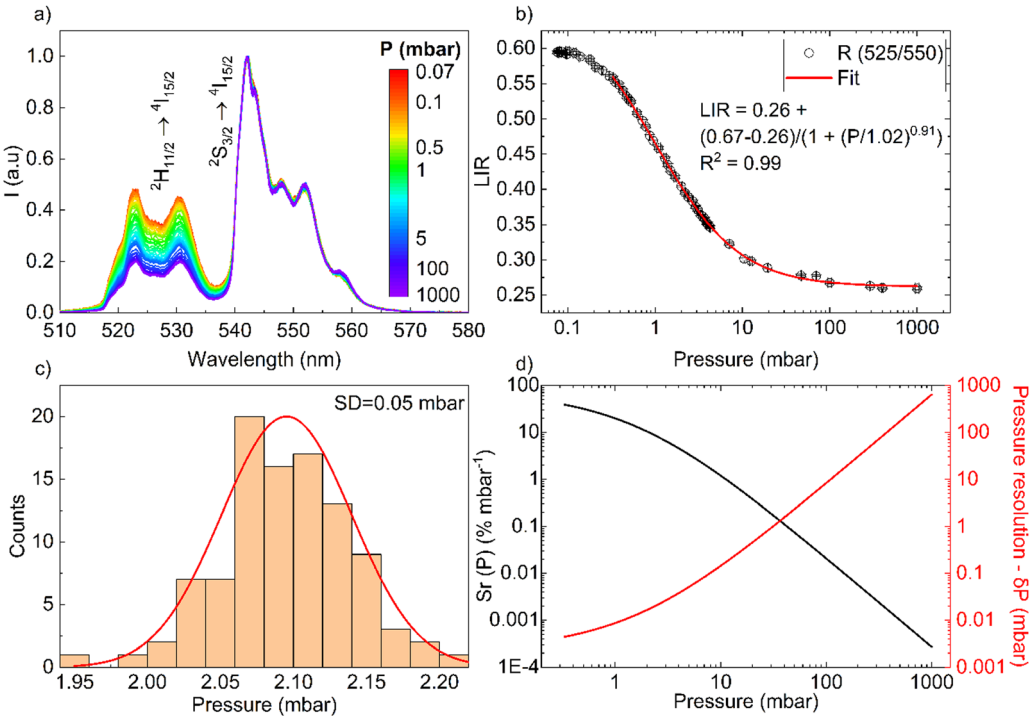

Fig. 5 (a) UC emission spectra of the $NaYF_4$:Gd^{3+}, Yb^{3+}, Er^{3+} material as a function of pressure, measured under (λ_{ex} = 975 nm and 20 W cm^{-2}). (b) Determined band intensity ratios as a function of pressure. (c) Histogram of the experimentally determined distribution of pressure values around 2 mbar. (d) Sensitivity and pressure sensing resolution as a function of pressure.

power (≈0.2–850 W cm^{-2}) and pressure (≈0.33–1000 mbar), ensuring accurate determination of the given quantities. In addition, for the detection of laser power, we developed a new bi-modal sensing strategy, using either the ratiometric approach or the single band emission intensity (525 nm) to improve the sensitivity of the material in the low power density regime. Another particularly important advantage of this sensor is its non-invasive character (remote detection), which allows detection in different environments. Moreover, it is also worth noting that this material presents the possibility of use as an optical nano-heater for various applications. Provided that to measure any of the three parameters, the other two must be controlled, otherwise it will induce a change in the LIR and it will not be known if it is due to a change in the study parameter. This study may be the beginning for a new class of sensors based on single compound for the multi-parameter detection of diverse temperature-dependent physical quantities.

Experimental section

Materials

All chemicals and reagents were commercially available and used without further purification unless otherwise stated. $Y(NO_3)_3{\cdot}6H_2O$ (99,99%), $Gd(NO_3)_3{\cdot}6H_2O$ (99,99%), $Yb(NO_3)_3{\cdot}5H_2O$ (99,99%), and $Er(NO_3)_3{\cdot}5H_2O$ (99,99%), were purchased from Sigma Aldrich, oleic acid from Fisher Chemicals, and NaOH (pellets) (99%) and NaF (99%), from Scharlau Chemie. For all experiments the ultra-pure, deionised water was used.

Synthesis

The UC nanoparticles were obtained following the modified procedure reported by Zhang *et al.*[43] At a first stage, 7.1 g of oleic acid was added to a 50 mL Erlenmeyer flask, followed by the addition of 0.7 g of NaOH (pellets) under vigorous stirring. After 2 minutes, 13 mL of ethanol was added and the suspension was heated to 30–40 °C in a water bath. Then, a solution of 300 mg of NaF (7.2 mmol) in 8.3 mL of deionized water was added to the reaction flask. When all reagents were completely dissolved, a solution of 1.12 mmol of $Ln(NO_3)_3$ [containing the following mole % of lanthanide ions: Y(III) 78%, Gd(III) 10%, Yb(III) 10%, and Er(III) 2%] in 1.5 mL of deionized water was added slowly with vigorous stirring. A white precipitate is formed and the suspension was heated to 40–50 °C for 10 min. Then, the suspension was placed in a hydrothermal autoclave reactor and heated to 230 °C for 12 hours. Once the reactor was cooled, the organic phase was decanted and discarded, and the solid material was washed with 25 mL of ethanol and centrifuged at 3000 rpm for 5 min. This process was repeated three times. Finally, the product was washed twice with 10 mL of deionized water and placed on a stove at 90 °C overnight.

Characterization

X-ray powder diffraction patterns were recorded at room temperature on a PANanalytical X'pert X-ray diffractometer with Cu K_α radiation (1.54184 Å). A transmission electron microscope (TEM), JEOL JEM 2100 with 0.24 nm resolution with an X-ray dispersive energy microanalyzer (EDX) Oxford X-MAX 80 mm^2

was used to identify the shape of the nanoparticles. UC emission spectra were recorded in the visible range using an Andor Shamrock 500 spectrometer, coupled to the Andor Newton silicon CCD camera. The excitation source was a tunable CW Ti:Sapphire laser system, Spectra Physics 3900S pumped with a 15 W 532 nm Spectra Physics Millenia, adjusted at 975 nm.

Measurements

For the all experiments, a pellet was made from the material ($\approx$260 μm thick) and placing the material on a small glass plate. For optical measurements of the sample as a function of temperature, the luminescence measurements were performed from 300 to 600 K using a tubular electric furnace (Gero RES-E 230/3), and a K-type thermocouple was used to control the temperature of the sample. In order to measure the laser power, a photodiode (Ophir StarLite) was used. Finally, for low pressure measurements, vacuum was obtained using an oil pump (Edwards RV3), where the manometer was connected to a digital controller (Edwards Active Gauge Controller Single Display).

Author contributions

C.H.A.: data curation, formal analysis, investigation, validation, writing – original draft. G. B. S.: investigation, writing – review & editing. I. R. M.: validation, investigation, project administration, supervision, writing – review & editing. J. S.: formal analysis, validation, writing – review & editing. K. S: data curation, writing – review & editing. K. S. C.: sotfware, writing – review & editing. Ł. M.: validation, writing – review & editing. M. R.: conceptualization, data curation, validation, funding acquisition, investigation, supervision, writing – review & editing.

Conflicts of interest

The authors declare no competing financial interest.

Acknowledgements

This work was financially supported by Ministerio de Ciencia e Innovacion of Spain (MICIIN) under the National Program of Sciences and Technological Materials (PID2019-106383GB-C44 and PID2019-107335RA-I00) and Gobierno de Canarias (PROID2021010102 and PROID2020010067) and EU-FEDER funds. M. R. acknowledges support from Fondo Social Europeo and Agencia Estatal de Investigación (RYC2020-028778-I/AEI/10.13039/501100011033).

References

1 Y. Fei and Y. Wang, *Rev. Mineral. Geochem.*, 2000, **41**, 521–557.
2 J. M. Recio, J. M. Menendez and A. Otero de la Roza, *An Introduction to High-Pressure Science and Technology*, CRC Press, Portland, 2016.
3 M. A. Antoniak, S. J. Zelewski, R. Oliva, A. Żak, R. Kudrawiec and M. Nyk, *ACS Appl. Nano Mater.*, 2020, **3**, 4209–4217.
4 S. Goderski, M. Runowski, P. Woźny, V. Lavín and S. Lis, *ACS Appl. Mater. Interfaces*, 2020, **12**, 40475–40485.
5 T. Tröster, *Handb. Phys. Chem. Rare Earths*, 2003, **33**, 515–589.
6 C. D. S. Brites, A. Millán and L. D. Carlos, *Handb. Phys. Chem. Rare Earths*, 2016, **49**, 339–427.
7 M. Runowski, A. Shyichuk, A. Tymiński, T. Grzyb, V. Lavín and S. Lis, *ACS Appl. Mater. Interfaces*, 2018, **10**, 17269–17279.
8 K. Dziubek, M. Citroni, S. Fanetti, A. B. Cairns and R. Bini, *J. Phys. Chem. C*, 2017, **121**, 2380–2387.
9 A. Katrusiak, *Acta Crystallogr., Sect. B: Struct. Sci., Cryst. Eng. Mater.*, 2019, **75**, 918–926.
10 M. Runowski, P. Woźny, S. Lis, V. Lavín and I. R. Martin, *Adv. Mater. Technol.*, 2020, **5**, 1901091.
11 K. Soler-Carracedo, I. R. Martin, M. Runowski, L. L. Martín, F. Lahoz, A. D. Lozano-Gorrín and F. Paz-Buclatin, *Adv. Opt. Mater.*, 2020, **8**, 2000678.
12 D. Jaque and F. Vetrone, *Nanoscale*, 2012, **4**, 4301–4326.
13 M. D. Dramićanin, *J. Appl. Phys.*, 2020, **128**, 40902.
14 P. Shi, Y. Duan, W. Wei, Z. Xu, Z. Li and T. Han, *J. Mater. Chem. C*, 2018, **6**, 2476–2482.
15 A. Bednarkiewicz, L. Marciniak, L. D. Carlos and D. Jaque, *Nanoscale*, 2020, **12**, 14405–14421.
16 J. G. Bünzli and C. Piguet, *Chem. Soc. Rev.*, 2005, **34**, 148–177.
17 M. Sato, S. W. Kim, Y. Shimomura, T. Hasegawa, K. Toda and G. Adachi, in *Chapter 278 – Rare Earth-Doped Phosphors for White Light-Emitting Diodes*, ed. B. Jean-Claude and P. Vitalij, Elsevier, 2016, p.1.
18 J. G. Buenzli, *Trends Chem.*, 2019, **1**, 751–762.
19 B. Golesorkhi, H. Nozary, A. Fürstenberg and C. Piguet, *Mater. Horiz.*, 2020, **7**, 1279–1296.
20 F. Maturi, C. Brites, R. Silva, K. Nigoghossian, D. Wilson, R. Ferreira, S. Ribeiro and L. Carlos, *Adv. Photonics Res.*, 2021, **3**, 2100227.
21 L. Marciniak, M. Szalkowski, A. Bednarkiewicz and K. Elzbieciak-Piecka, *J. Mater. Chem. C*, 2022, **10**, 11040–11047.
22 R. G. Geitenbeek, H. W. de Wijn and A. Meijerink, *Phys. Rev. Appl.*, 2018, **10**, 064006.
23 P. Du, L. Luo, H. Park and J. S. Yu, *Chem. Eng. J.*, 2016, **306**, 840–848.
24 P. Du, L. Laihui, W. Li, Y. Qingying and H. Chen, *Appl. Phys. Lett.*, 2014, **104**, 152902.
25 M. Runowski, P. Woźny, N. Stopikowska, I. R. Martin, V. Lavín and S. Lis, *ACS Appl. Mater. Interfaces*, 2020, **12**, 43933–43941.
26 S. V. Rashchenko, A. Kurnosov, L. Dubrovinsky and K. D. Litasov, *J. Appl. Phys.*, 2015, **117**, 145902.
27 T. Zheng, M. Runowski, P. Woźny, S. Lis and V. Lavín, *J. Mater. Chem. C*, 2020, **8**, 4810–4817.
28 M. Runowski, P. Woźny, V. Lavín and S. Lis, *Sens. Actuators, B*, 2018, **273**, 585–591.
29 Y. Wang, T. Seto, K. Ishigaki, Y. Uwatoko, G. Xiao, B. Zou, G. Li, Z. Tang, Z. Li and Y. Wang, *Adv. Funct. Mater.*, 2020, **30**, 2001384.
30 H. K. Mao, J. Xu and P. M. Bell, *J. Geophys. Res.*, 1986, **91**, 4673–4676.
31 A. Dewaele, M. Torrent, P. Loubeyre and M. Mezouar, *Phys. Rev. B: Condens. Matter Mater. Phys.*, 2008, **78**, 104102.

32 F. Datchi, A. Dewaele, P. Loubeyre, R. Letoullec, Y. L. Godec and B. Canny, *High Press. Res.*, 2007, **27**, 447–463.
33 J. W. Gregory, K. Asai, M. Kameda, T. Liu and J. P. Sullivan, *Proc. Inst. Mech. Eng., Part G*, 2008, **222**, 249–290.
34 S. M. Peak and A. N. Watkins, *ACS Appl. Nano Mater.*, 2020, **3**, 9813–9821.
35 P. Cortelletti, A. Skripka, C. Facciotti, M. Pedroni, G. Caputo, N. Pinna, M. Quintanilla, A. Benayas, F. Vetrone and A. Speghini, *Nanoscale*, 2018, **10**, 2568–2576.
36 A. Benayas, E. Hemmer, G. Hong and D. Jaque, *Near Infrared-Emitting Nanoparticles for Biomedical Applications*, Springer International Publishing AG, Cham, 2020.
37 C. D. S. Brites, K. Fiaczyk, J. F. C. B. Ramalho, M. Sójka, L. D. Carlos and E. Zych, *Adv. Opt. Mater.*, 2018, **6**, 1701318.
38 S. Balabhadra, M. L. Debasu, C. D. S. Brites, R. A. S. Ferreira and L. D. Carlos, *J. Phys. Chem. C*, 2017, **121**, 13962–13968.
39 K. Trejgis, A. Bednarkiewicz and L. Marciniak, *Nanoscale*, 2020, **12**, 4667–4675.
40 L. Marciniak, K. Elzbieciak-Piecka, K. Kniec and A. Bednarkiewicz, *Chem. Eng. J.*, 2020, 388, 124347.
41 M. Runowski, Pressure and Temperature Optical Sensors: Luminescence of Lanthanide-Doped Nanomaterials for Contactless Nanomanometry and Nanothermometry, in *Handbook of Nanomaterials in Analytical Chemistry*, ed. C. M. Hussain, Elsevier, 2020, pp. 227–273.
42 M. Runowski, P. Woźny and I. R. Martín, *J. Mater. Chem. C*, 2021, **9**, 4643–4651.
43 F. Zhang, Y. Wan, T. Yu, F. Zhang, Y. Shi, S. Xie, Y. Li, L. Xu, B. Tu and D. Zhao, *Angew. Chem., Int. Ed.*, 2007, **46**, 7976–7979.
44 K. Zheng, K. Y. Loh, Y. Wang, Q. Chen, J. Fan, T. Jung, S. H. Nam, Y. D. Suh and X. Liu, *Nano Today*, 2019, **29**, 100797.
45 H. Fujii, *Private Communication*, Central Research Laboratory Hitachi Limited, Tokyo, Japan, 1975.
46 J. F. Suyver, J. Grimm, M. K. van Veen, D. Biner, K. W. Krämer and H. U. Güdel, *J. Lumin.*, 2006, **117**, 1–12.
47 M. M. Lage, R. L. Moreira, F. M. Matinaga and J. Gesland, *Chem. Mater.*, 2005, **17**, 4523–4529.
48 C. Renero-Lecuna, R. Martín-Rodríguez, R. Valiente, J. González, F. Rodríguez, K. W. Krämer and H. U. Güdel, *Chem. Mater.*, 2011, **23**, 3442–3448.
49 R. A. Janjua, C. Gao, R. Dai, Z. Sui, M. A. Ahmad Raja, Z. Wang, X. Zhen and Z. Zhang, *J. Phys. Chem. C*, 2018, **122**, 23242–23250.
50 M. Pollnau, D. R. Gamelin, S. R. Lüthi, H. U. Güdel and M. P. Hehlen, *Phys. Rev. B: Condens. Matter Mater. Phys.*, 2000, **61**, 3337–3346.
51 Y. Lei, H. Song, L. Yang, L. Yu, Z. Liu, G. Pan, X. Bai and L. Fan, *J. Chem. Phys.*, 2005, **123**, 174710.
52 M. Runowski, P. Woźny, S. Lis, V. Lavín and I. R. Martin, *Adv. Mater. Technol.*, 2020, **5**, 1901091.
53 B. Zelelow, G. E. Khalil, G. Phelan, B. Carlson, M. Gouterman, J. B. Callis and L. R. Dalton, *Sens. Actuators, B*, 2003, **96**, 304–314.
54 M. Runowski, N. Stopikowska, D. Szeremeta, S. Goderski, M. Skwierczyńska and S. Lis, *ACS Appl. Mater. Interfaces*, 2019, **11**, 13389–13396.
55 M. Skwierczyńska, N. Stopikowska, P. Kulpiński, M. Kłonowska, S. Lis and M. Runowski, *Nanomaterials*, 2022, **12**, 1926.
56 T. Zheng, M. Runowski, P. Woźny, B. Barszcz, S. Lis, M. Vega, J. Llanos, K. Soler-Carracedo and I. R. Martín, *J. Alloys Compd.*, 2022, **906**, 164329.
57 N. Rakov and G. S. Maciel, *Sens. Actuators, B*, 2012, **164**, 96–100.
58 M. L. Debasu, D. Ananias, I. Pastoriza-Santos, L. M. Liz-Marzán, J. Rocha and L. D. Carlos, *Adv. Mater.*, 2013, **25**, 4868–4874.
59 V. Kumar, S. Som, S. Dutta, S. Das and H. C. Swart, *RSC Adv.*, 2016, **6**, 84914–84925.
60 H. Lv, P. Du, L. Luo and W. Li, *Mater. Adv.*, 2021, **2**, 2642–2648.
61 J. W. Gregory, H. Sakaue, T. Liu and J. P. Sullivan, *Annu. Rev. Fluid Mech.*, 2014, **46**, 303–330.